$$\overline{u_i' u_j'} = \overline{u_i' u_j'}^{(l)} + \overline{u_i' u_j'}^{(b)} . \qquad [39]$$

These turbulent correlations are considered to have significant importance in bubble migration, and therefore in phase distribution.

For homogeneous potential bubbly flows, the Bieshevel & van Winjgaarden's (1984) results are widely used. They demonstrated that the pseudo-turbulence stress tensor is given by

$$\overline{u_i' u_j'}^{(b)} = \frac{3}{20}\alpha \|\mathbf{U}_r\|^2 \delta_{ij} + \frac{1}{20}\alpha \overline{\mathbf{U}_{ri}\mathbf{U}_{rj}} , \qquad [40]$$

where α is the void fraction, and the relative velocity between the liquid and bubble is given by

$$\mathbf{U}_r = \mathbf{u}_l - \mathbf{u}_b . \qquad [41]$$

For the turbulence of the liquid, a widely used approach is the k-ε model, and variations of it.

5.3. Nodalization and conditional sampling

In this experimental investigation, 81 sets of data were acquired. Each set consisted of 27 frames resulting in a total of 2187 frames for the experiment. Figure 16 shows the distribution of the bubble centroids for the whole experiment on the XY plane. This figure clearly shows the anisotropy of the bubble paths during rising. The bubbles were released at the pipe center.

The data sets were divided into groups having similar bubble trajectories to perform conditional sampling. A similar trajectory is that in which the bubble, in its rising path, within the viewing test volume, passes through the same region (locations) in at least 3 of 4 frames, in which the bubble was present in the viewing volume. The nodalization scheme for the bubble position in the viewing volume is illustrated in figure 17a. The horizontal plane was divided into five regions. The circle segment number 1 is at the center of the pipe, with a radius of 2.25 mm. The annulus region was divided into four segments, 2, 3, 4, and 5, as shown in the figure. The axial nodalization consists of four segments, each with a size of ΔZ_b = 2.75 mm. For the liquid phase data, the measurement volume is divided into a 3D grid of 9×9×9 in the X-, Y-, and Z-

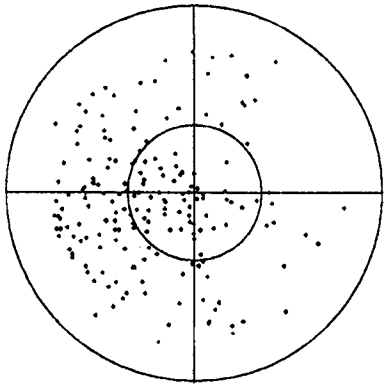

Figure 16. Projection of the distribution of the bubble centroids for the experiment of 240 images on the XY plane. The anisotropy of the bubble paths during rising within the test volume should be noted. The bubbles were released at the pipe center.

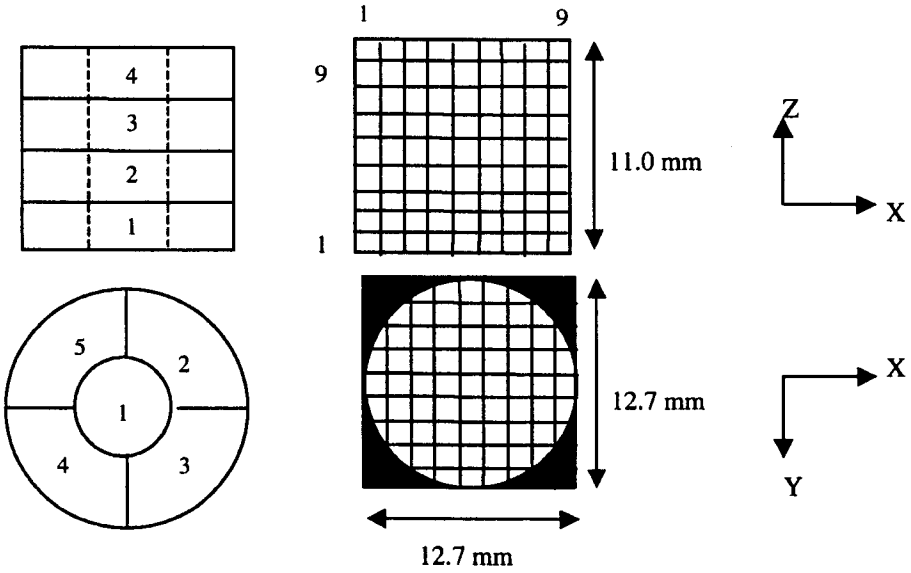

Figure 17. Nodalization of the test section. (a) Gas; and (b) liquid phases. For the air bubble, the nodalization has been established considering an average equivalent bubble diameter of 3 mm, and its location is determined by its centroid.

directions, respectively. The total number of the cells is 729, although only 621 fall inside the pipe. The size of the node for ΔX and ΔY is equal to 1.41 mm and for ΔZ = 1.22 mm. Figure 17b illustrates the nodalization used for the analysis of the liquid phase data. The distribution of various trajectories was as follows: 17.3% of the bubbles followed trajectory 111; 2.5% of the rising paths were trajectory 222; 3.7% of the bubbles traveled trajectory 333; 19.8% had bubble trajectory 444; and 18.5% had trajectory 555. The rest of the rising paths were a combination of trajectories.

Once the velocity fields were determined for each separated bubble trajectory, and in order to better quantify the wall influence in the structure of the flow, and to obtain more samples for the averaging operation, the nodalization scheme for bubble position in the test volume was then considered of consisting of only two zones in the horizontal plane. Namely, one zone close to the wall as regions 2, 4, and 5, and a zone far from the wall as region 1, see figure 17a. The value of the radius dividing both regions was set to 2.25 mm (same as above). This value was chosen as optimum after studying the bubble's trajectory for all of the data sets. The regions in the pipe annulus were all rotated to coincide to the third quadrant ($x < 0$ and $y < 0$) in the horizontal plane, assuming symmetry of the flow fields, so an average for all trajectories close to the wall could be performed. The bubble trajectory close to the pipe wall consequently occurred 44.5% of the experiment.

An example of bubble trajectory 111 is depicted in figure 18. This figure clearly indicates that the bubble trajectories were not straight paths for this experiment. The actual trajectory of the bubble in figure 18 is 1112. A similar figure for a trajectory close to the wall is shown in figure 19. For this figure, the actual trajectory is 4445. The Reynolds number of the bubbles, $\mathrm{Re}_b = \rho_l U_b d_b / \mu_l$, was in a range from about 350 to 700. At this range, a bubble freely rising in stagnant water exhibits oscillating motion along the rising path, and shape change. The predicted shape is ellipsoidal, although not necessarily symmetric. The motion is expected to be helical and/or zigzag, and even with a rocking motion. The helical paths along with the rocking motion, and the ellipsoidal shape, were observed in this experiment with both the combined PIV and shadow images, as it can clearly be seen in figures 18 and 19.

By combining the bubble data for a specified trajectory, we obtained an average flow field, for each instant in time. The conditional average velocity was obtained through

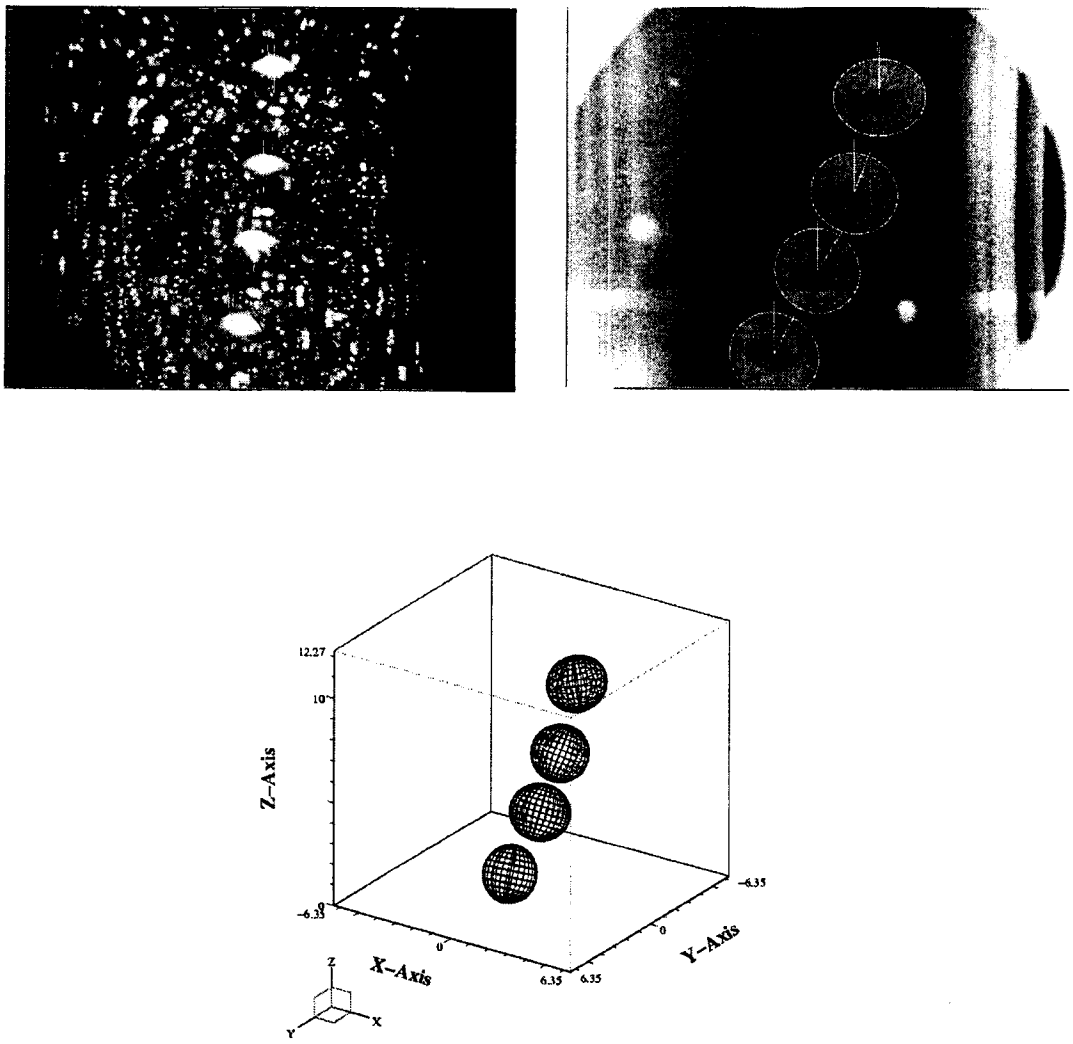

Figure 18. Example of bubble trajectory at the center of the pipe. The two-dimensional projections of the trajectory from the Center and Shadow cameras, and the three-dimensional bubble reconstructions are shown. Actual trajectory is 1112.

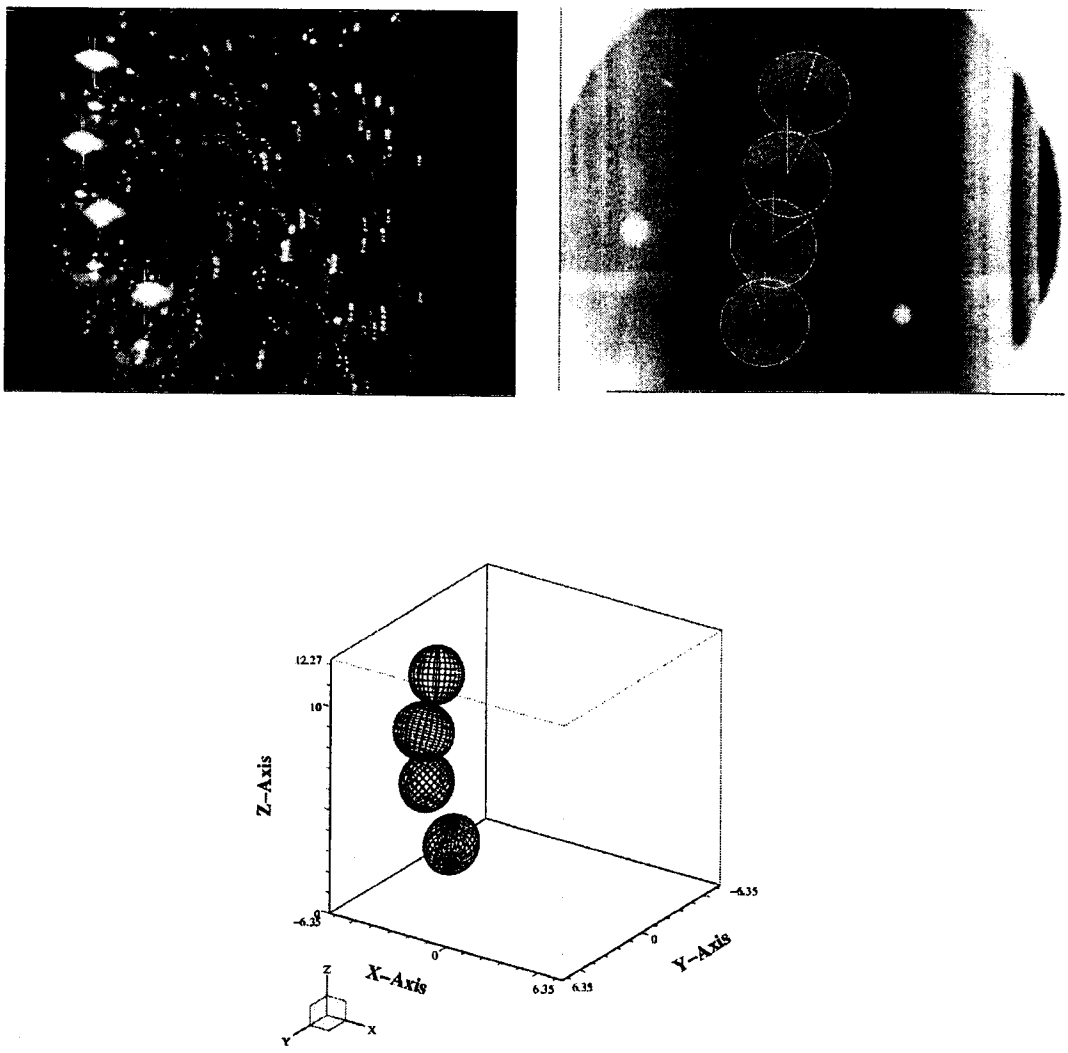

Figure 19. Example of bubble trajectory along the pipe wall. The two-dimensional projections of the trajectory from the Center and Shadow cameras, and the three-dimensional bubble reconstructions are shown. Actual trajectory is 4445.

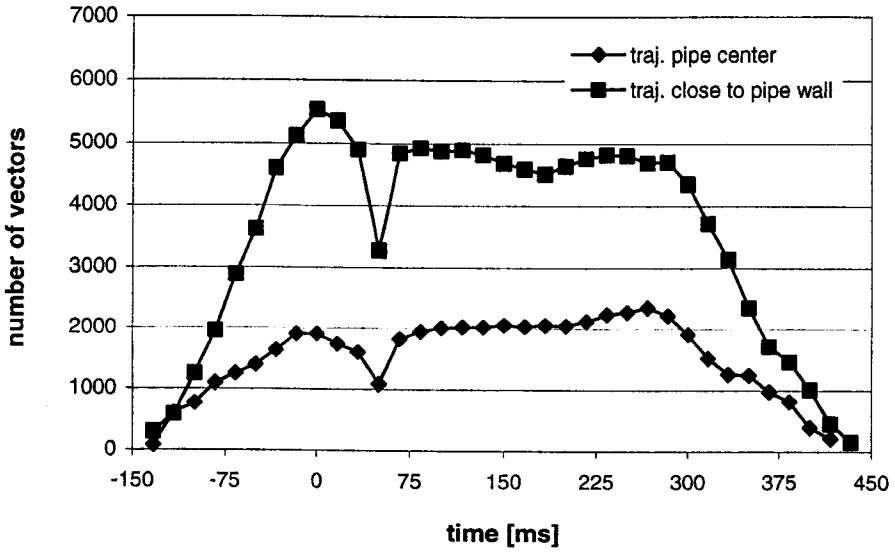

Figure 20. Total number of vectors used for the averaging operation at each time step for both bubble trajectories. $t = 0$ is the first frame in which the bubble appears in the viewing volume.

$$\overline{u}(x,y,z,t) = \frac{1}{n}\left\{\sum_{i=1}^{n} u_i(x,y,z,t) \;\middle|\; \begin{matrix}\text{specified}\\ \text{bubble}\\ \text{trajectory}\end{matrix}\right\}. \qquad [42]$$

The total number of vectors for each time step for the trajectories in the pipe center and close to the wall is shown in figure 20. Clearly, from figure 20, only the time interval from t = -75 ms to about t = 375 ms can be considered to have enough vectors to yield reliable results. The averaged flow field was interpolated in the regions in which no velocity vectors were found. The interpolation algorithm is based on the Hardy scheme (Hardy 1990; Blanchat 1992), which performs a biquadratic interpolation.

5.4. Mean flow field description

Due to the three-dimensionality and unsteadiness of the flow behavior, 3D plots of all parameters are needed to better understand of the flow structure. Figures 21a to 24a present the

distribution of the mean kinetic energy for the four frames in which the bubble is present in the viewing volume, for the bubble trajectories rising along the pipe center. These frames correspond to t_p = 0 ms, t_p = 16.67 ms, t_p = 33.3 ms, and t_p = 50.0 ms, respectively. Similarly, figures 21b to 24b show the distribution of the magnitude of the vorticity in the test volume. Observe that the areas of higher mean kinetic energy coincide with the areas of higher vorticity magnitude, in general. This is explained as follows. For this bubble trajectory, at the instant of the bubble presence in the viewing volume, practically all of the liquid flow is restricted to a space from about one bubble diameter, d_b, to two d_b between the bubble boundary and the pipe wall, in the horizontal plane. Due to the incompressibility of the water, the flow experiences acceleration to compensate for the smaller flow area available. The areas surrounding the bubble, therefore, are the ones where the mean kinetic energy and vorticity reach higher values, as clearly seen in the respective figures. The flow closer to the bubble travels upstream surrounding the bubble's primary wake, and collides at the end of the wake, close to the center of the pipe. This collided flow generates a flow barrier, which decelerates any flow passing through it. It should be noted that a symmetric flow is not expected. This is because the bubble did not rise in a straight trajectory. In addition, ellipsoidal shape and rocking motion were observed. Similar results were observed for the trajectories close to the pipe wall. That is, the higher values of the mean kinetic energy and vorticity magnitude are found close to the bubble, see figures 25a to 28a, and 25b to 28b, respectively. The flow in the radial direction apart from the bubble with a distance more than one bubble diameter is practically undisturbed, reducing its magnitude as it gets closer to the pipe wall.

The influence zone of the bubble is different for these two trajectories. For trajectory along the pipe core, the bubble influence reaches downstream to an average distance of two bubble diameters, from the bubble's top. This can be seen in figure 21. For the bubble trajectories close to the pipe wall, the bubble influence downstream on the flow field reaches greater distances in comparison with the cases of bubbles rising along the pipe core. As it can be seen in figure 25, the downstream influence reaches to an average of 3 d_b. This is so because the increase of the acceleration of the liquid flow between the bubble surface and the pipe wall is limited due to the wall friction effect. This friction overcomes the momentum transfer from the bubble to the liquid. Consequently, the bubble pushes up liquid that experiences this resistance. Subsequent liquid layers are then pushed further up.

The bubble's primary wake for trajectories along the pipe center extends 3 d_b upstream, from

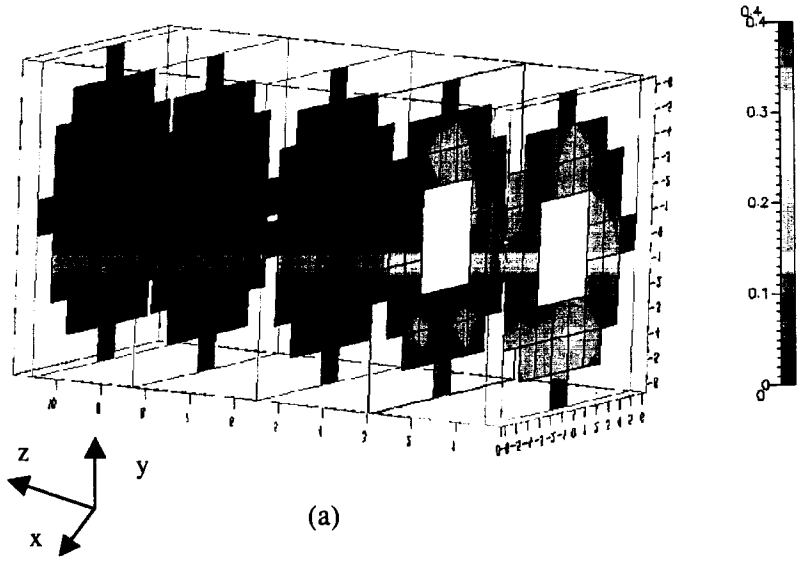

(a)

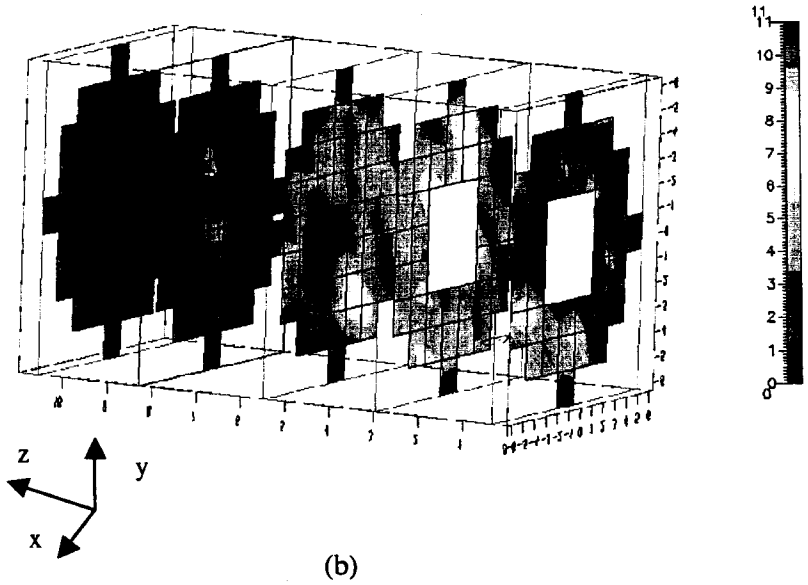

(b)

Figure 21. Distribution of a) mean kinetic energy, in μJ; and b) vorticity magnitude, in Hz, at $t_p = 0$ ms. Bubble rising along the pipe center.

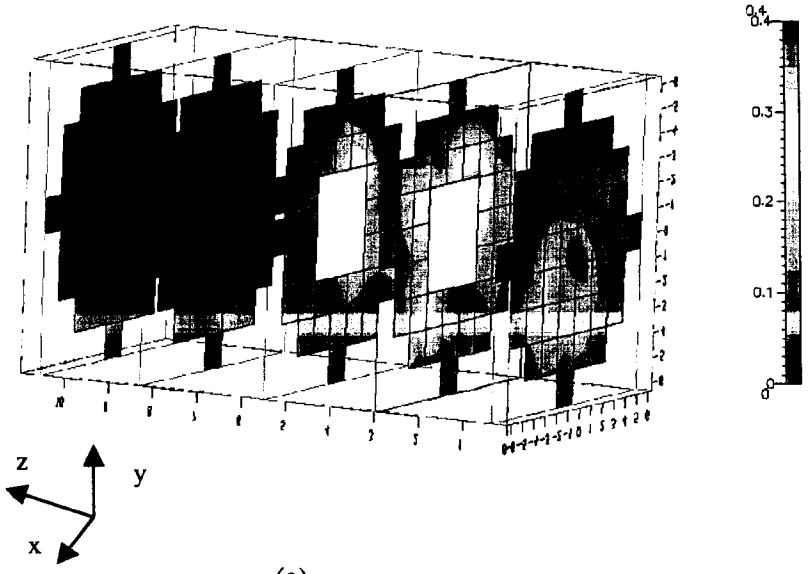

(a)

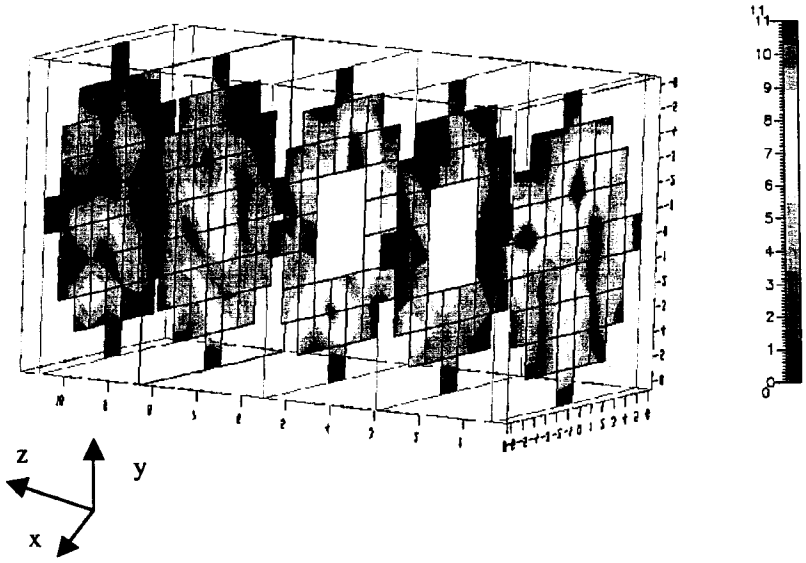

(b)

Figure 22. Distribution of a) mean kinetic energy, in μJ; and b) vorticity magnitude, in Hz, at t_p = 16.67 ms. Bubble rising along the pipe center.

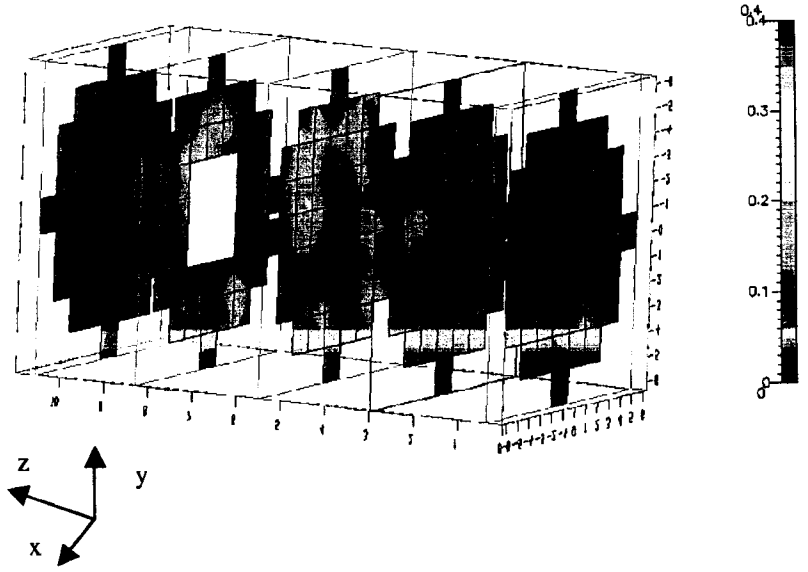

(a)

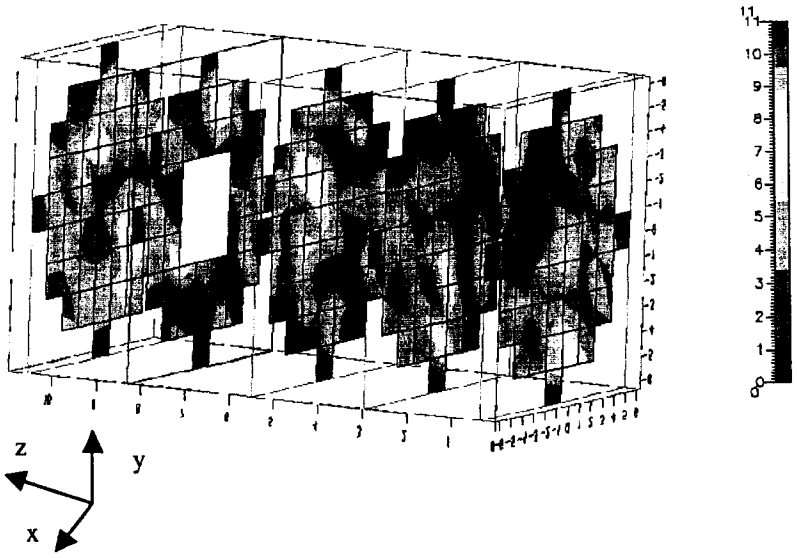

(b)

Figure 23. Distribution of a) mean kinetic energy, in μJ; and b) vorticity magnitude, in Hz, at t_p = 33.33 ms. Bubble rising along the pipe center.

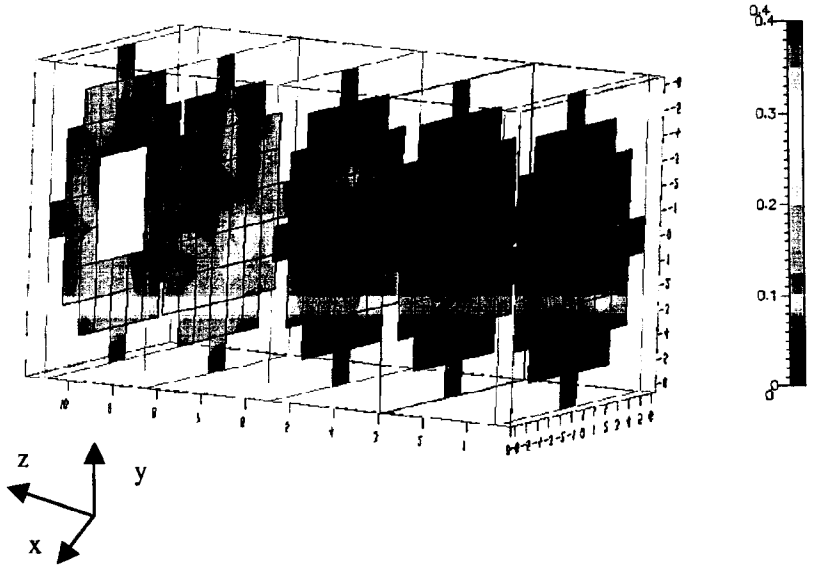

(a)

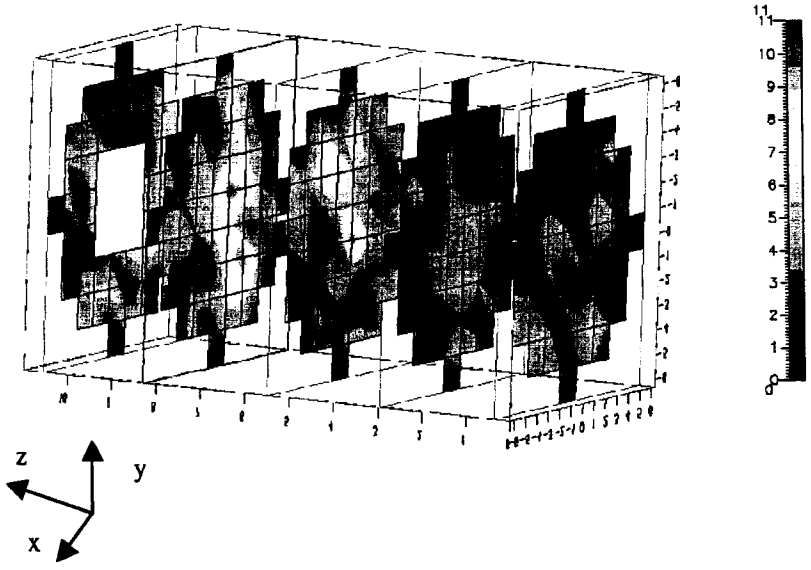

(b)

Figure 24. Distribution of a) mean kinetic energy, in μJ; and b) vorticity magnitude, in Hz, at t_p = 50.0 ms. Bubble rising along the pipe center.

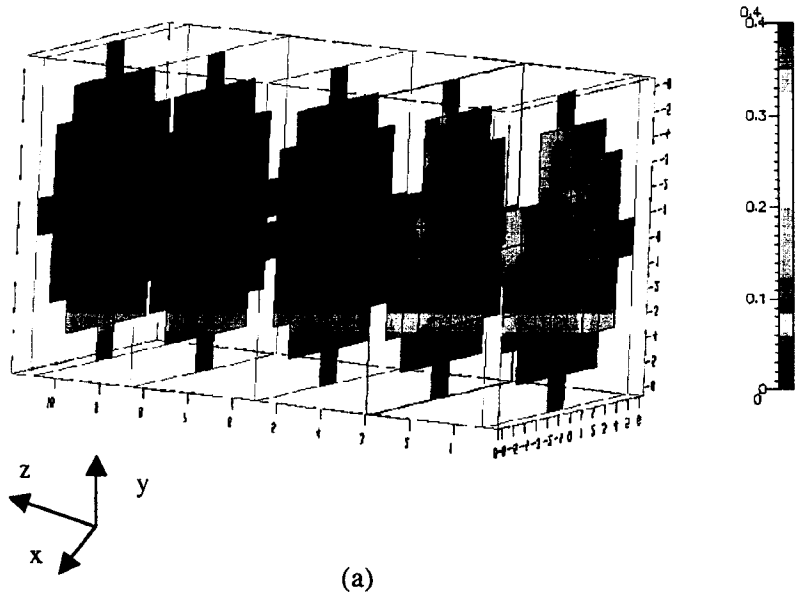

(a)

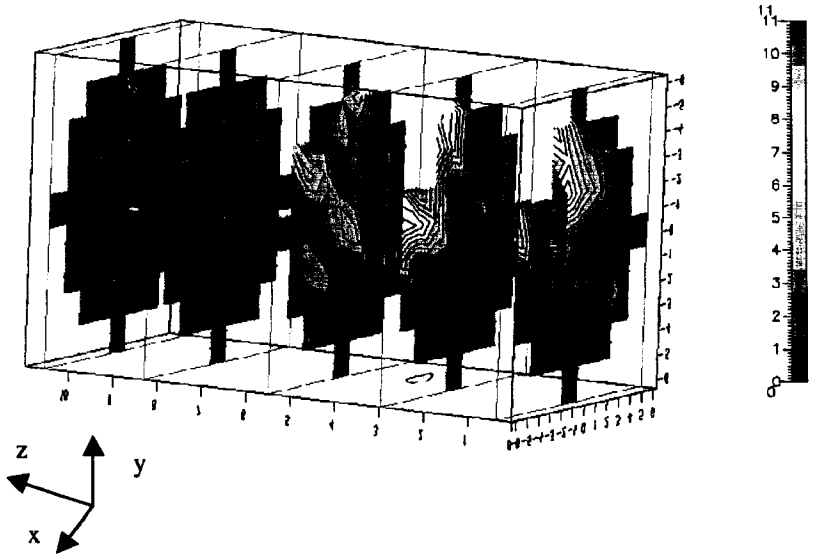

(b)

Figure 25. Distribution of a) mean kinetic energy, in μJ; and b) vorticity magnitude, in Hz, at $t_p = 0$ ms. Bubble trajectory close to the pipe wall.

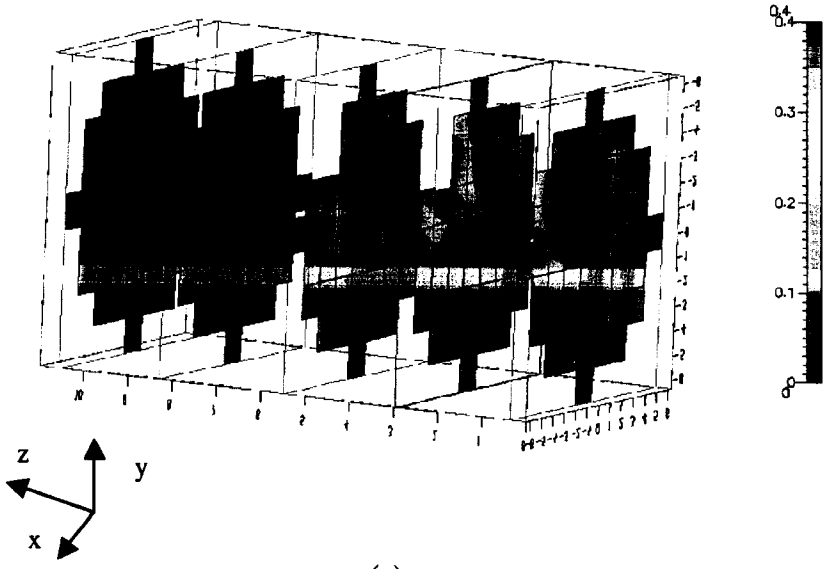

(a)

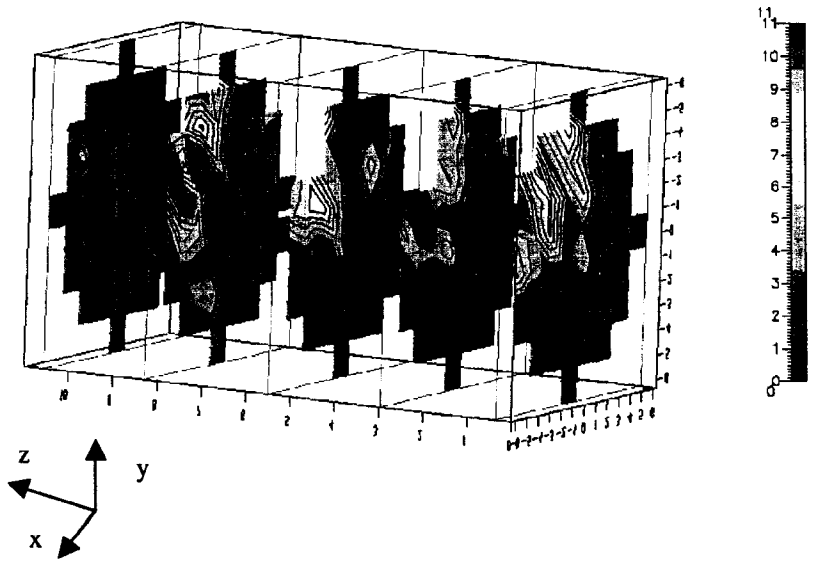

(b)

Figure 26. Distribution of a) mean kinetic energy, in μJ; and b) vorticity magnitude, in Hz, at t_p = 16.67 ms. Bubble trajectory close to the pipe wall.

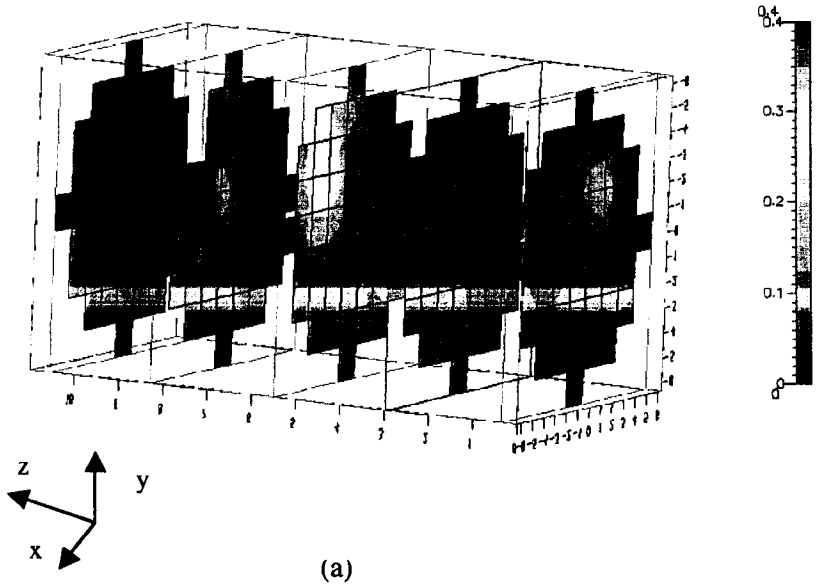

(a)

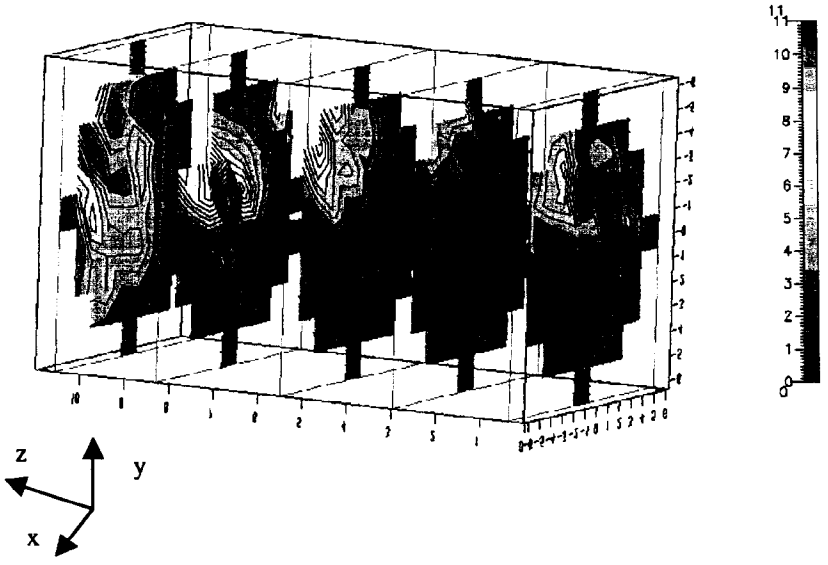

(b)

Figure 27. Distribution of a) mean kinetic energy, in μJ; and b) vorticity magnitude, in Hz, at t_p = 33.33 ms. Bubble trajectory close to the pipe wall.

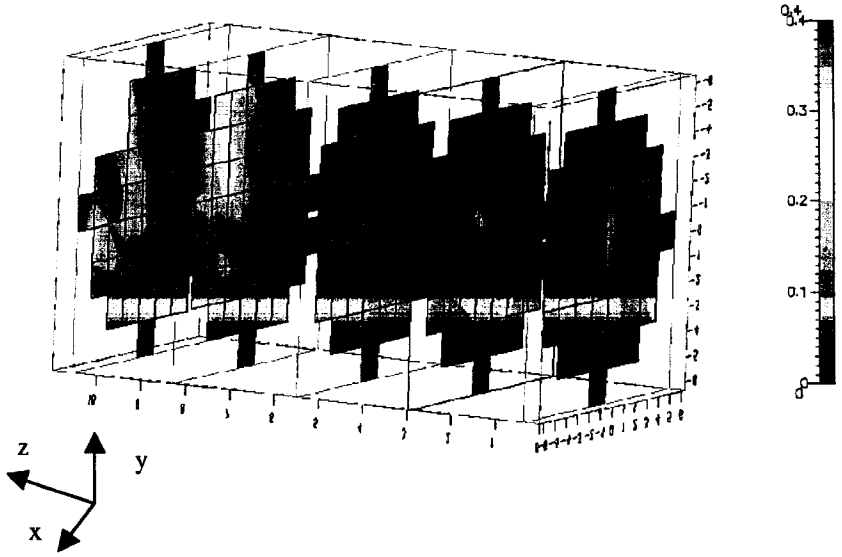

(a)

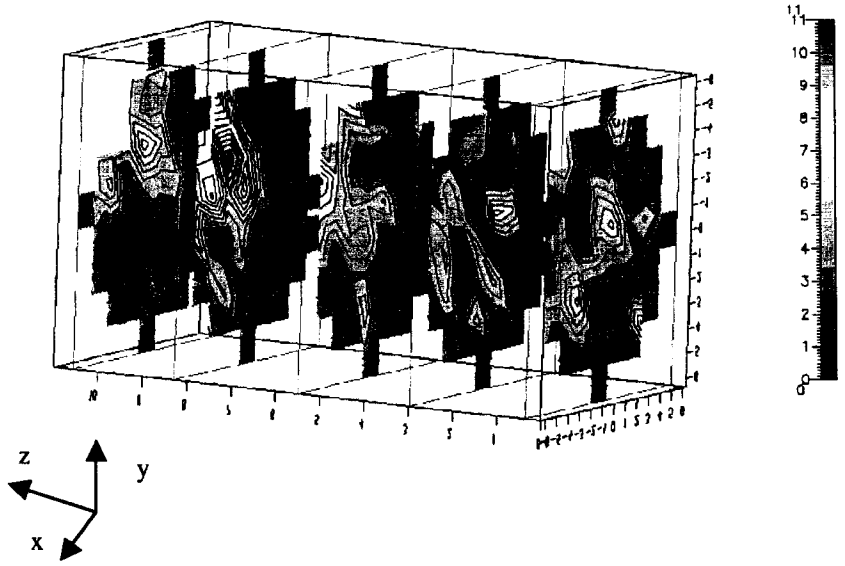

(b)

Figure 28. Distribution of a) mean kinetic energy, in μJ; and b) vorticity magnitude, in Hz, at t_p = 50.0 ms. Bubble trajectory close to the pipe wall.